

See discussions, stats, and author profiles for this publication at: <https://www.researchgate.net/publication/313186294>

Hybrid parameter identification of a multi-modal underwater soft robot

Article in *Bioinspiration & Biomimetics* · January 2017

DOI: 10.1088/1748-3190/aa5ccc

CITATIONS

36

READS

633

5 authors, including:



Francesco Giorgio Serchi

The University of Edinburgh

59 PUBLICATIONS 676 CITATIONS

[SEE PROFILE](#)



Andrea Arienti

3DNextech s.r.l.

26 PUBLICATIONS 1,050 CITATIONS

[SEE PROFILE](#)



Francesco Corucci

Scuola Superiore Sant'Anna

24 PUBLICATIONS 422 CITATIONS

[SEE PROFILE](#)



Michele Giorelli

Magneti Marelli

26 PUBLICATIONS 1,297 CITATIONS

[SEE PROFILE](#)

Some of the authors of this publication are also working on these related projects:



I-Support: ICT-Supported Bath Robots [View project](#)



Soft Multi-body Dynamics [View project](#)

Hybrid parameter identification of a multi-modal underwater soft robot

This content has been downloaded from IOPscience. Please scroll down to see the full text.

Download details:

IP Address: 193.205.81.18

This content was downloaded on 01/02/2017 at 13:58

Manuscript version: Accepted Manuscript

Giorgio-Serchi et al

To cite this article before publication: Giorgio-Serchi et al, 2017, Bioinspir. Biomim., at press:

<http://dx.doi.org/10.1088/1748-3190/aa5ccc>

This Accepted Manuscript is copyright Copyright 2017 IOP Publishing Ltd

During the embargo period (the 12 month period from the publication of the Version of Record of this article), the Accepted Manuscript is fully protected by copyright and cannot be reused or reposted elsewhere.

As the Version of Record of this article is going to be / has been published on a subscription basis, this Accepted Manuscript is available for reuse under a CC BY-NC-ND 3.0 licence after a 12 month embargo period.

After the embargo period, everyone is permitted to use all or part of the original content in this article for non-commercial purposes, provided that they adhere to all the terms of the licence

<https://creativecommons.org/licences/by-nc-nd/3.0>

Although reasonable endeavours have been taken to obtain all necessary permissions from third parties to include their copyrighted content within this article, their full citation and copyright line may not be present in this Accepted Manuscript version. Before using any content from this article, please refer to the Version of Record on IOPscience once published for full citation and copyright details, as permissions will likely be required. All third party content is fully copyright protected, unless specifically stated otherwise in the figure caption in the Version of Record.

When available, you can view the Version of Record for this article at:

<http://iopscience.iop.org/article/10.1088/1748-3190/aa5ccc>

Hybrid parameter identification of a multi-modal underwater soft robot

F. Giorgio-Serchi¹, A. Arienti², F. Corucci^{3,4}, M. Giorelli³
& C. Laschi³

¹ Fluid Structure Interaction Research Group, University of Southampton,
Southampton SO16 7QL, UK

² 3DNextech s.r.l., Livorno, Italy

³ The Biorobotics Institute, Scuola Superiore Sant'Anna, Pontedera, Italy

⁴ Morphology, Evolution & Cognition Lab, Vermont Complex Systems Center,
University of Vermont, Burlington, VT, USA

E-mail: F.Giorgio-Serchi@soton.ac.uk

June 2016

Abstract. We introduce an octopus-inspired, underwater, soft-bodied robot capable of performing waterborne pulsed-jet propulsion and benthic legged-locomotion. This vehicle consists for as much as 80% of its volume of rubber-like materials so that structural flexibility is exploited as a key element during both modes of locomotion. The high bodily softness, the unconventional morphology and the non-stationary nature of its propulsion mechanisms require dynamic characterization of this robot to be dealt with by *ad-hoc* techniques. We perform parameter identification by resorting to a hybrid optimization approach where the characterization of the dual ambulatory strategies of the robot is performed in a segregated fashion. A Least Squares-based method coupled with a Genetic Algorithm-based method is employed for the swimming and the crawling phases, respectively. The outcomes bring evidence that compartmentalized parameter identification represents a viable protocol for multi-modal vehicles characterization. However, the use of static thrust recordings as the input signal in the dynamic determination of shape-changing self-propelled vehicles is responsible for critical underestimation of the quadratic drag coefficient.

Keywords: soft robotics, underwater robots, multi-modal locomotion, aquatic propulsion, legged locomotion, parameter identification

Submitted to: *Bioinspir. Biomim.*

1. Introduction

Underwater operations have become of primary importance in several fields of application in the marine and maritime sector, such as deep-sea oil drilling, offshore platform installation and rescue operations. This requires underwater vehicles to perform increasingly complex tasks in ever more daunting scenarios. More and more often the need arises for underwater vehicles to undertake interventions in dangerous scenarios, where the need to operate in deep and cluttered environments is unattainable by divers. In order to address these challenges, new breeds of robots are being developed. Standard underwater robots, commonly referred to as Unmanned Underwater Vehicles (UUVs), can be categorized into Autonomous Underwater Vehicles (AUVs) and Remotely Operated Vehicles (ROVs) [1]. While AUVs are more commonly employed for monitoring tasks over open stretches of sea, at present most intervention and maintenance operations are performed by ROVs.

Despite their widespread employment in the offshore industry, UUVs are subject to major limitations associated with their bulk and lack of structural flexibility. The capability of this class of vehicles to operate at close proximity with submerged structures is often challenged by the difficulty to establish a safe interaction with the surrounding, especially when exposed to current or wave dominated climates. This is a common occurrence, for instance, in the installation and maintenance operations of marine renewable energy plants, [2]. In response to the increased complexity of the tasks which UUVs are faced with, enhancement of the capabilities and efficiency of UUVs has been looked into via the incremental improvement of traditional technology. This has entailed, for instance, to endow standard AUVs with the capability to hover, by relieving ROV-like vehicles from the burden of the tether, [3], or by improving navigation and positioning systems, [4].

Alternatively, bioinspired principles have been employed in the design of underwater vehicles in order to enhance propulsion performances, manoeuvring skills and sensing abilities, [5]. The study of organisms capable of tackling multi-domain locomotion is also of primary importance in the strive for designing more advanced and versatile machines [6, 7]. More recently, the attempt has been made to account for the compliant nature and the multi degrees of freedom

(DoF) bending capability of the organisms from which inspiration is drawn, [8]. This allows these vehicles to withstand large deformations and in this way establish a compliant interaction with the environment. The development of machines endowed with continuously deforming soft structures and actuators, commonly referred to as soft robotics [9], is a new approach which could have a significant impact in the context of offshore operations.

Indeed, in terrestrial environments the advantages of a soft body are partially balanced by remarkable hindrances. As a consequence, although softness appears to have a functional role in most animals,

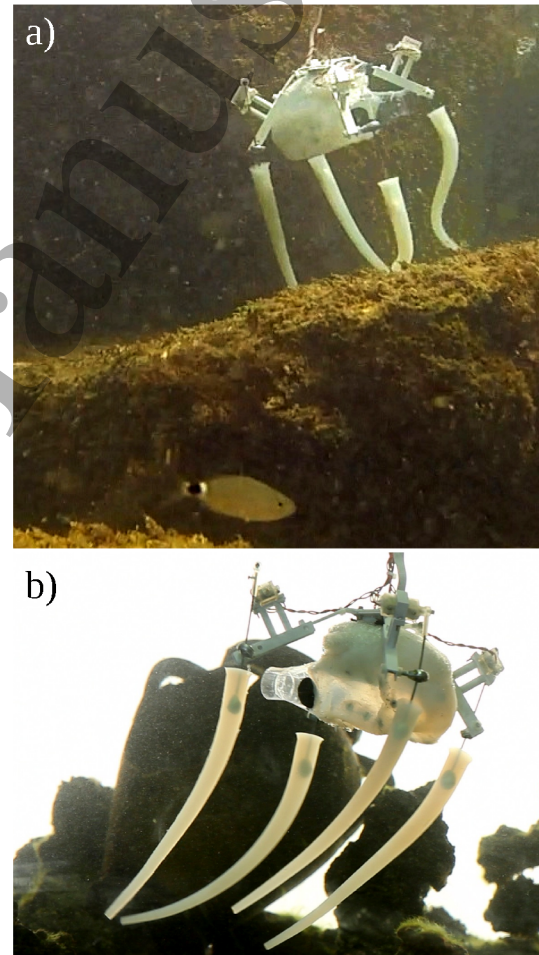


Figure 1. The multi-modal soft-bodied aquatic robot PoseiDRONE [10] during crawling (a) and swimming (b). Credit to "The Age of Robots" by M. Brega.

1
2
3
4
5
6
7
8
9
10
11
12
13
14
15
16
17
18
19
20
21
22
23
24
25
26
27
28
29
30
31
32
33
34
35
36
37
38
39
40
41
42
43
44
45
46
47
48
49
50
51
52
53
54
55
56
57
58
59
60

the examples of completely soft-bodied terrestrial organisms are limited in number and size. On the contrary, in the aquatic environment there is a wealth of soft-bodied organisms, heterogeneous both in size and kind, characterized by locomotor performances that are comparable to those of aquatic vertebrates. This suggests that the aquatic environment may be congenial for emphasizing the advantages of soft bioinspired robots [11, 12].

Taking the cue from this, the authors have developed a new kind of soft robot for underwater applications: the PoseiDRONE [10], Fig. 1. The robot, inspired by octopodes and composed for the most part of flexible rubber-like materials, is robust, cheap, small-sized and lightweight. Its multi-modal locomotion, which integrates crawling by means of soft-limbs and pulsed-jet swimming, provides the chance to employ it both as a sea-bottom crawler as well as a sea-dwelling vehicle. The soft nature of this vehicle enables it to handle interactions with the surrounding environment by relying on its own structural compliance rather than on accurate control.

However, the complex morphology of the robot, along with its largely unsteady modes of locomotion, make the determination of the whole-body dynamics and hence the control problem especially hard to deal with. A rigorous definition of the key elements which characterize this vehicle during its crawling and swimming dynamics is thus of primary importance. As a consequence, we resort to the experimental determination of the dynamics of the vehicle by means of a hybrid Least Squares/Genetic Algorithm (LSGA) parameter identification approach. This method entails treating the vehicle as two distinct systems based on the mode of locomotion employed and applying the direct Least Squares (LS) method or the Genetic Algorithm-based (GA) method respectively to the swimming and the crawling regimes.

The work is presented according to the following outline: first the overall design of the vehicle is illustrated, separately addressing the swimming and the crawling unit. Then experiments performed with the whole robotic system are presented, followed by the identification procedure established respectively for the swimming and crawling modes of locomotion.

2. Robot Design

PoseiDRONE was developed by combining design principles from soft robotics and biomimetics, electing cephalopods as the source of inspiration. The robot consists of a single platform onto which a crawling and a swimming unit are joint, thus enabling multi-modal locomotion. The system relies on four flexible limbs for legged-locomotion and a pulsed-jet thruster

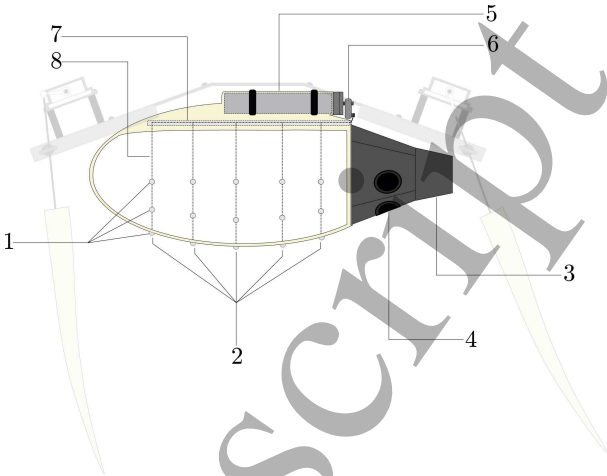


Figure 2. Schematic representation of the PoseiDRONE swimming unit: (1) cable attachment points over the elastic shell, (2) axial location of the cross sections subject to cable traction, (3) the nozzle, (4) inflow valves, (5) the motor, (6) the crank, (7) the axial pulley which distributes the cable over the various cross sections, (8) the cables.

for waterborne propulsion, both of which are made of silicone. Each of these elements is linked to a rigid, cross-shaped aluminium frame, which supports the motors used to actuate the soft limbs. The overall weight of the robot is 0.75 kg, and 80% of its volume is composed of silicone, providing the vehicle with high structural flexibility. The casts and the rigid parts were manufactured via 3D FDM printing with ABS. In order to enable aquatic operation of the vehicle, surfaces were made homogeneous and waterproof via the 3DFinisher acetone vapour treatment (3DNextech s.r.l).

The structural compliance of the vehicle is a key element during the swimming and crawling routines. During the former, the actuation entails the inflation and deflation of a deformable chamber whose elastic response mediates the recursive occurrence of this cyclic routine. In addition, the ability of the vehicle to undergo volume variation thanks to its soft nature is known to provide significant positive feedback on thrust, [13, 14]. During crawling, limbs flexibility is exploited to handle the contact with the ground, eliminating the need for fine and continuous control of the limb position and making the legged-locomotion robust.

2.1. Swimming Unit

Waterborne propulsion of the robot is dealt with by pulsed-jet propulsion. The thrusting unit operates in analogy to what cephalopods (i.e. octopuses and squids) do to swim, see [15]: an elastic chamber is sequentially deflated and inflated thus driving a succession of expulsion and ingestion stages of ambient fluid. This process enables the vehicle to expel finite

slugs of water which, by conservation of momentum, propel the vehicle in the direction opposite to the jet. This mode of aquatic propulsion has lately attracted the interest of the research community due to its association with impulse-rich discontinuous jets [16] and hence its aptness for designing agile vehicles. The thrusting unit (Fig. 2) employed in the present work, introduced in [17], benefits from the assets provided by pulsed-jet propulsion [18] while reducing the adoption of rigid components, thus preserving the previously mentioned advantages of a soft body.

The thruster is a hollow shell 160 mm long, made of EcoFlex-0030 silicone. The collapse of this elastic chamber is executed throughout the whole axial extent of the shell by placing five cable attachment points, element (1) in Fig. 2, at four sections along the axis of the shell, element (2) in Fig. 2. At each cross section the five cables are attached, at one end, to the wall of the rubber shell and are gathered, at the other end, through a fixed pulley located in the upper part of the hollow chamber, element (7) in Fig. 2. In the present thrusting unit, the fixed pulley is immersed in the silicone mould located in the dorsal part of the vehicle. The shortening of the cables is due to the rotation of a crank which, by pulling the cable attachment points, deforms the shell into a lobe-shaped geometry, squeezing water through the nozzle, for details see [19].

This thrusting unit is capable of ejecting 120 mL of the fluid stored within the chamber at unstrained state, corresponding to $\sim 34\%$ of its initial volume. The refill stage passively exploits the elastic energy of the strained walls of the vehicle—a good example of how suitable material properties can simplify control [20]—and is facilitated by three umbrella valves located around the base of the nozzle, element (4) in Fig. 2. The motor which acts upon the cables allows the vehicle to pulse within the range of 0.8 to 1.5 pulsations per second (pps).

2.2. Crawling Unit

The design of the crawling unit elaborates on the foundations of bioinspired legged locomotion by exploiting passively compliant soft limbs, in order to achieve robust benthic locomotion over fragile and irregular substrates.

Bioinspired legged locomotion relies on the eccentric trajectory of the feet in order to achieve the forward displacement of the body, [21, 22]. The classical mechanisms which enable to replicate such kind of trajectory are the four-bar [23] or the three-bar linkage mechanisms. In PoseiDRONE we employ a modified three-bar mechanism where structural compliance in the distal bar is introduced, element (3) in Fig. 3 and 4. Beside enabling a gentle interaction with the substrate, limb compliance has been found to

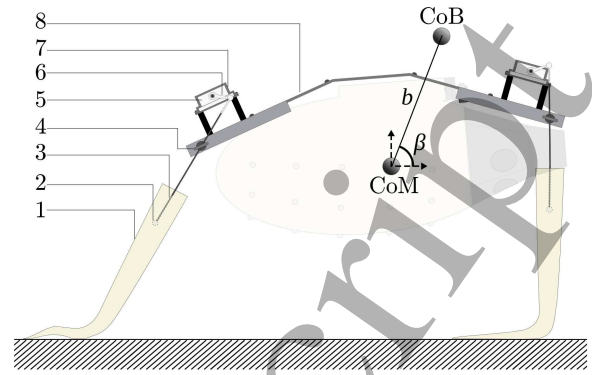


Figure 3. Schematic representation of the PoseiDRONE crawling unit: (1) the flexible limbs, (2) plastic element facilitating the adhesion of the steel cable within the silicone limb, (3) the steel cable, (4) spherical bearing (allows translation and rotation), (5) the motor, (6) the crank, (7) the motor case and (8) the aluminium frame supporting the limbs and the thruster.

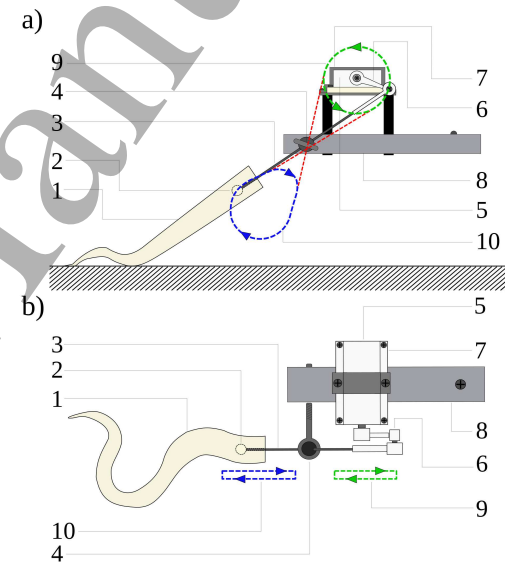


Figure 4. A schematic of the three-bar mechanism during the limb actuation routine: (a) side view and (b) top view. The elements depicted represent: (1) the flexible limbs, (2) plastic element facilitating the adhesion of the steel cable within the silicone limb, (3) the steel cable, (4) the spherical bearing for the steel cable, (5) the motor, (6) the crank, (7) the motor case, (8) the aluminium frame supporting the limbs and the thruster, (9) upper crank circular loop and (10) lower crank eccentric loop.

support enhanced stability of the locomotion [24].

Each of the soft limbs consists of a conic, rubber-like unit, element (1) in Fig. 3 and 4, with a flexible cylindrical bar, a steel cable, embedded in the limb principal axis, element (3). The motion is transmitted to each of the limbs by a dedicated three-bar mechanism which drives the distal bar into an eccentric loop, element (10) in Fig. 4. This, along with the structural compliance of the limb, mediates the routine described below (Fig. 4): the arm adheres

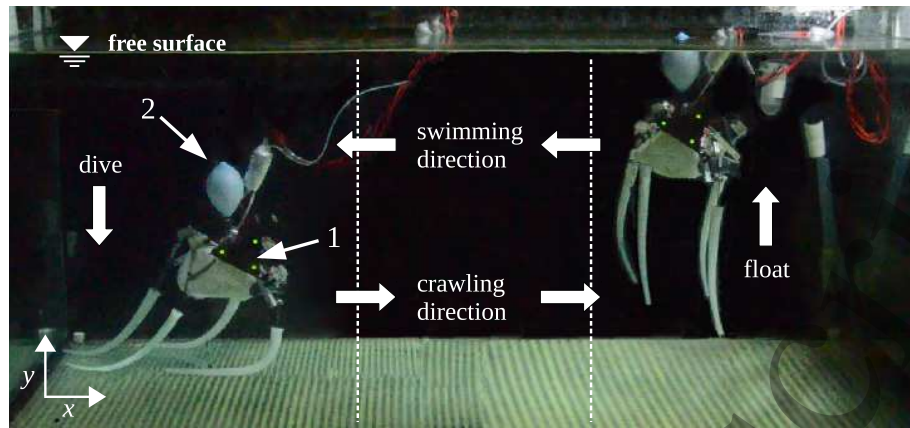


Figure 5. Experimental test setup. The experiments entail the vehicle swimming to the end of the tank, then diving to the bottom, crawling towards the opposite end of the tank and eventually surfacing. The highlighted elements are: (1) the LED-markers for 3d tracking and (2) the controllable buoyancy module.

to the surface, it pushes against the ground and eventually detaches from it, thus enabling the cycle to start over. The geometry of the three-bar mechanism was tuned in order for the distal part of the leg to maximize the extent of the push while at the same time easing a clearance condition in the detachment phase.

The mechanism was developed with a combination of commercial and purposely manufactured parts. A 21 mm crank is 3D printed in acrylonitrile butadiene styrene (ABS) and an ABS hollow rod lodges a steel cable of diameter 2 mm and length 10 mm, which in turn is embedded into a cone of EcoFlex-0030 silicone. The third element of the mechanism is the rigid frame of the robot, element (8) in Fig. 3 and 4, made of a 2 mm thick foil of aluminium alloy 6061. As for the actuation, each limb is driven by a dedicated GM12a Solarbotics DC motor housed inside a waterproof resin holder, element (7). The crank is connected to the driving shaft on one side and to the connecting hollow rod on the other by means of a low friction cylindrical joint. The steel cable is also constrained by a spherical bearing which enables rotation and translation, element (2) in Fig. 3 and 4. This spherical bearing allows the arm to flex in every direction to fully exploit its compliance.

3. Experimental Methods

A series of experiments were devised in order to assess the vehicle performance during multi-modal locomotion and to provide a dataset to be used for parameter identification. Two kind of tests were performed: locomotion analysis and thrust measurements. Both of these were performed in a 1150 mm long, 590 mm wide and 500 mm deep tank filled with salt water.

During locomotion analysis an inflatable buoyancy module was fitted to the dorsal part of the robot, see element (2) in Fig. 5. By varying the inflation state of the buoyancy module, the mean density of the robot was determined, thus enabling it to heave across the water column. Swimming was performed by setting the overall relative density of the robot to 0.97 with respect to that of the surrounding medium, whereas, crawling tests were performed in different settings (details in what follows) characterized by a relative density greater than 1. The tests entailed the routine depicted in Fig. 5: the vehicle would swim from one end of the tank to the opposite one, then dive to the bottom of the tank, it would then crawl back to the opposite end wall and eventually rise to the initial position.

Motion analysis was based on the three dimensional motion tracking of the robot. Three markers, see

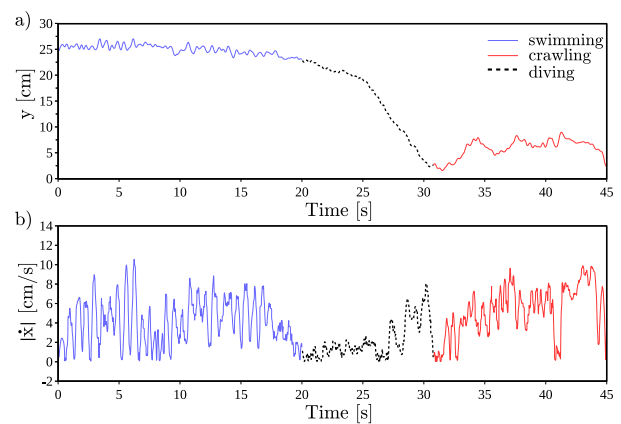


Figure 6. Results from a prototypical locomotion test. In (a), the displacement along the vertical direction of the CoM is reported and in (b) the surge speed. The colours highlight the swimming, diving and crawling phase.

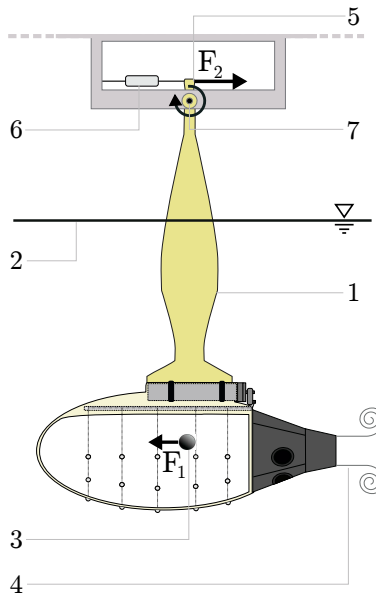


Figure 7. Experimental setup for thrust measurement: (1) the shaft which links the force sensor to the vehicle, (2) the level of the free surface, (3) the centre of mass (CoM) of the vehicle, (4) the issuing jet of fluid, (5) the point of application of the reaction force to thrust generation, (6) the force sensor and (7) the pivot of the shaft.

element (1) in Fig. 5, were fitted to the moving body and eight additional ones were placed in the tank at the boundaries of the workspace. High-speed cameras were employed to track the position of the markers, and in this way derive the displacement of the CoM of the robot. The Direct Linear Transformation (DLT) technique was then applied in order to transform two 2D images in a single 3D representation. This provided a full state of the robot consisting of x , y and z positions of the CoM as well as of roll, yaw and pitch angles.

During swimming the tests were repeated at a motor angular velocity ranging from 5.0 to 15.0 rad/s, i.e. from 0.8 to 1.5 pulsations per second (pps). During crawling each leg was actuated at a constant speed of ~ 12.6 rad/s and the tests were repeated by varying the mean body density (ρ_r) and the position of the buoyancy module, i.e. the distance b and angle β between the CoM and the Centre of Buoyancy (CoB), see Fig. 3. This resulted in the robot attaining a variety of different stances during crawling and, thus, different gaits which ranged from quadrupedal crawling to bipedal locomotion [25, 24]. The fastest configuration ($\rho_r = 1238 \text{ kg/m}^3$, $b = 0.09 \text{ m}$, $\beta = 12.6^\circ$) was retained for parameter identification. This corresponds to a bipedal gait [26] in which the robot exhibited a mean speed $\bar{x} = 4.4 \text{ cm/s}$ (with 0.24 cm/s standard deviation).

An example from one of these experiments is reported in Fig. 6. Here the displacement of the CoM of the robot during translation across the tank

is displayed, Fig. 6(a). During the first 20 s the robot is floating, and the swimming routine is active; between ~ 20 s to 30 s the buoyancy module is being deflated, letting the vehicle sink to the tank bottom. After this, the crawling routine is activated, as highlighted by the marked oscillations of the CoM. Similarly, Fig. 6(b) depicts the magnitude of the surge velocity during these three phases. The oscillatory speed recorded during the sinking stage at ~ 30 s is determined by the robot establishing contact with the ground.

Further experiments were performed to estimate the thrust force generated by the pulsed-jet actuator, which was later used as input signal to the model in the parameter identification for the swimming dynamics. Fig. 7 shows the experimental rig developed to perform such measurements. The vehicle, fully submerged in ambient fluid, was fixed to a shaft, element (1) in Fig. 7, which constrains the motion to a pure rotation about the pivot, element (7) in Fig. 7. Friction is limited by a low resistance bearing in the pivot. Upon thruster activation, the force experienced by the vehicle is transferred to the load cell, (6) in Fig. 7, an S-beam Futek (FSH00103). The sensor has a maximum capacity of 22 N and a sensitivity of 2 mV/V; in addition the load cell is coupled with an amplifying module Mecol 2039 Ministrain.

An example of one of these tests is reported in Fig. 8, where the information concerning the motor (motor speed, position and current) and the resulting thrust are depicted. Based on the actuator design, the propulsion routine entails the motor pulling the cables for half of its rotation and releasing them for the remaining half [19]. The elastic shell is thus subject to cable-driven collapse (during which fluid is expelled across the nozzle) and then spontaneously inflates due to potential elastic energy (sucking in ambient fluid through the valves and the nozzle). This routine is observed in the recordings: at 0° , element (1) in Fig. 8(a), the motor starts pulling the cables, which drive the collapse of the shell and the expulsion of fluid. This is confirmed by the motor speed decreasing, the current increasing and by the occurrence of positive peaks of thrust, Fig. 8(b). Once the motor has reached 180° the expulsion of fluid has terminated and the maximum amount of expellable fluid has been ejected, giving rise to the major thrust peak, element (2) in Fig. 8. After this the shell starts to inflate, driving water inside the chamber through the nozzle which causes negative thrust to occur.

4. Identification methods

In order to formulate a model-based controller for the robot [27], or to guide and inform future designs by means of simulation studies [28, 29, 30, 31], the

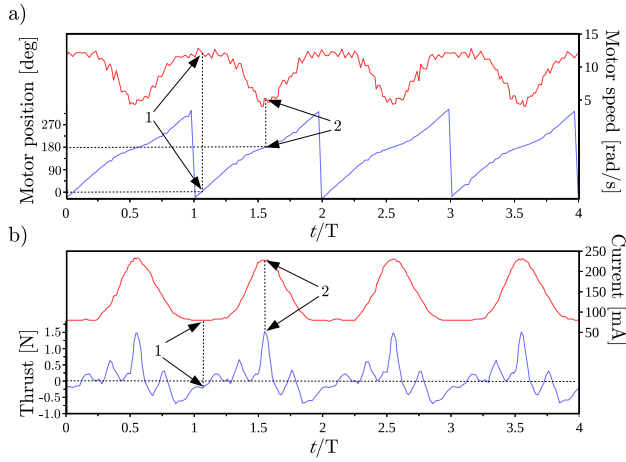


Figure 8. Combined recordings from the force sensor and the motor encoder for the thrust measurement tests. In (a) the motor speed, in red, and the motor shaft position, in blue, throughout a series of pulsations. The indexes (1) and (2) respectively point at the instants when expulsion of fluid start and terminates. In (b) the current absorbed by the motor, red, and the thrust measured by the force sensors, blue.

identification of unknown model parameters is of primary importance. This procedure aims at finding a set of parameters that allow model equation to faithfully predict the behavior of the robot, minimizing the discrepancies between predicted and observed behavior. As a consequence, this procedure is usually based on an optimization algorithm which attempts to match the dynamics predicted by the equations to that observed during experimental tests performed in comparable environmental conditions, [32].

Because of the marked distinction between the two modes of locomotion, parameter identification was dealt with separately for the crawling and swimming phases. This is motivated by the two operative conditions being clearly separated, never overlapping, dependent on different parameters and characterized by largely different dynamics. A first difference between the two regimes is related to hydrodynamic parameters. While, during the swimming phase, border effects can be neglected, this does not hold in the crawling phase, where the robot is very close to the substrate. Another difference is entailed by the immersion state of the buoyancy module: almost completely immersed in the crawling phase, partially immersed in the swimming phase. This clearly affects both the added mass and the drag coefficients. The dynamics of the robot is also considerably different in the two regimes: while in the swimming phase the robot translates along the x direction, during crawling the robot undergoes heave and pitch oscillations. As a consequence, the number, the type and the value of relevant parameters differ in the two locomotions.

We resort to an identification procedure which we

refer to as hybrid LSGA approach based on the direct Least Squares (LS) method for the swimming phase and on a Genetic Algorithm (GA) for the crawling phase. The procedure for both routines entails a training stage and a testing stage. In the former, the actual identification occurs, eventually outputting the estimated parameters. The latter entails the testing of these parameters in a different configuration from that of the identification. These analyses are performed at quasi-steady state regime.

4.1. Swimming Dynamics Identification

The equation governing the dynamics of a neutrally buoyant body swimming along the surge direction x , is described by eq.(1).

$$\tilde{m}\dot{x} = -\Lambda\dot{x}|\dot{x}| + \tau \quad (1)$$

where \dot{x} is the velocity in the surge direction and $\tilde{m} = M + m_{a_s}$ is the effective mass comprising of the inertia of the robot M and its added mass m_{a_s} during swimming. The drag acting on the swimming vehicle is based on the ensemble viscous quadratic drag coefficient Λ , while τ is the pulsed-jet thrust generated by the cyclic routine of inflation and deflation of the silicone shell, as reported in Fig. 8(b).

Model equations governing the swimming phase, eq.(1), thus require the identification of m_{a_s} and Λ . To do so, data extracted from thrust measurements (section 3) are used as input signal in eq.(1). This yields a velocity profile which can be readily compared to the one extracted from locomotion analysis of the freely swimming vehicle. Validation of the estimated parameters is achieved by means of the mismatch between the estimated velocity and the real velocity of the robot measured in tank experiments. Eq. (1) is linear in the parameters, thus enabling the employment of the Least Squares method. The direct version of the Least Squares method from [33] was implemented, and the velocity signal directly adopted, avoiding the need of numerically deriving the acceleration. The swimming phase identification process was performed as follows.

Thrust analysis: thrust measurements are performed at various pulsation frequencies (from 0.8 to 1.5 pps) in order to cover the same range of pps employed during locomotion analysis. Thrust generation in the soft-bodied actuator presented in section 2.1 has been found to exhibit a highly non-linear behavior due to its dependence on the elastic response of the shell during the refill stage [34, 19]. Hence experimental measurements are needed as a reliable estimate of the input signal for the identification procedure, Fig. 9(a) and Fig. 10(a).

Filtering: noise in the experiment recordings arise from sources such as wave reflections from the tank

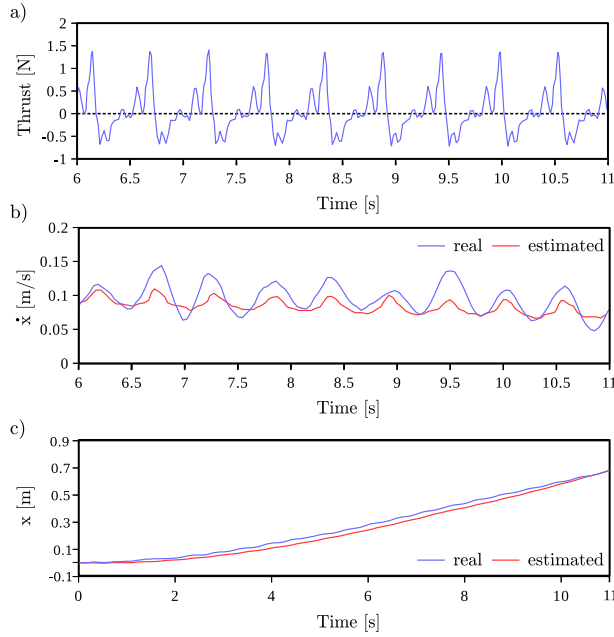


Figure 9. Swimming phase training set: (a) pulsed-jet thrust input signal for the identification; (b) surge speed at quasi-steady swimming regime; (c) CoM surge displacement throughout the whole experiment.

walls and vibration of the tether. In order to reduce these, velocity signals were treated with a Savitzky-Golay filter.

Test selection: two trials were chosen to build the training and the test set. These were selected by making sure that analogous frequencies had been recorded in the thrust experiments.

Parameter identification: the identification data set composed by the pair vectors (\dot{x}, τ) was used to apply the direct version of the Least Squares method, whose implementation (based on [33]) is briefly described in the following.

The hydrodynamics equation which describe the surge motion, eq.(1), can be rewritten as follows:

$$\ddot{x} = -\frac{\Lambda}{\tilde{m}}\dot{x}^2 + \frac{\tau}{\tilde{m}} = \alpha\dot{x}^2 + \gamma\tau = [\dot{x}^2 \ \tau] \cdot [\alpha \ \gamma]^T \quad (2)$$

with $\alpha = -\Lambda/\tilde{m}$ and $\gamma = \tau/\tilde{m}$. The identification data set is composed of N samples (\dot{x}_k, τ_k) , corresponding to the values of the signals (\dot{x}, τ) at discrete time instants t_k . Eq.(2) can be integrated between two generic subsequent time instants t_k and t_{k+1} yielding:

$$\int_{t_k}^{t_{k+1}} \ddot{x} dt = \left[\int_{t_k}^{t_{k+1}} \dot{x}^2 dt \quad \int_{t_k}^{t_{k+1}} \tau dt \right] \cdot [\alpha \ \gamma]^T \quad (3)$$

By approximating the integral with the rectangle method, the previous equation can be rewritten as follows:

$$\dot{x}_{k+1} - \dot{x}_k = [\dot{x}_k^2(t_{k+1} - t_k) \ \tau_k(t_{k+1} - t_k)] \cdot [\alpha \ \gamma]^T \quad (4)$$

If the signals are uniformly discretized, the difference between two subsequent time instants is equal to the interval h , therefore the previous equation can be simplified as follows:

$$\dot{x}_{k+1} - \dot{x}_k = h [\dot{x}_k^2 \ \tau_k] \cdot [\alpha \ \gamma]^T \quad (5)$$

Considering the N samples which compose the identification set, the previous equation can be expanded to N rows in the following manner:

$$\underbrace{\begin{bmatrix} \dot{x}_1 - \dot{x}_0 \\ \dot{x}_2 - \dot{x}_1 \\ \dots \\ \dot{x}_N - \dot{x}_{N-1} \end{bmatrix}}_{\mathbf{y}} = h \underbrace{\begin{bmatrix} \dot{x}_0^2 & \tau_0 \\ \dot{x}_1^2 & \tau_1 \\ \dots & \dots \\ \dot{x}_{N-1}^2 & \tau_{N-1} \end{bmatrix}}_{\mathbf{H}} \cdot \underbrace{\begin{bmatrix} \alpha \\ \gamma \end{bmatrix}}_{\boldsymbol{\theta}} \quad (6)$$

Solution for the vector $\boldsymbol{\theta}$ thus reads,

$$\hat{\boldsymbol{\theta}} = (\mathbf{H}^T \mathbf{H})^{-1} \mathbf{H}^T \mathbf{y}. \quad (7)$$

The standard deviation can be computed as,

$$\hat{\sigma}_{\theta} = \sqrt{\text{diag}((\mathbf{H}^T \mathbf{H})^{-1}) \sigma_{\epsilon}^2} \quad (8)$$

where the term σ_{ϵ}^2 is the variance of the zero mean Gaussian measurement noise, which can be estimated as:

$$\hat{\sigma}_{\epsilon}^2 = \frac{(\mathbf{y} - \mathbf{H}\hat{\boldsymbol{\theta}})^T (\mathbf{y} - \mathbf{H}\hat{\boldsymbol{\theta}})}{\text{dim}(\mathbf{y}) - \text{dim}(\boldsymbol{\theta})} \quad (9)$$

In order to validate the estimation $\hat{\boldsymbol{\theta}}$, the percentile parameter error $p_{\hat{\boldsymbol{\theta}}} = 100(\hat{\sigma}_{\theta})/|\hat{\boldsymbol{\theta}}|$ was finally computed, [35].

Test: the testing phase consisted in comparing the velocity predicted by the model (provided with identified parameters and a given thrust signal, i.e. Fig. 9(a) and Fig. 10(a)) with the real velocity of the robot recorded in a tank experiment. The error between the real and the estimated velocity signals was then calculated and a statistical analysis was conducted on the error signal.

4.2. Swimming phase results

By applying the identification procedure for the swimming phase, the parameter vector $\hat{\boldsymbol{\theta}}$, the standard deviation $\hat{\sigma}_{\theta}$ and the percentile parameter error $p_{\hat{\boldsymbol{\theta}}}$ were computed (Tab. 1). In order to validate the parameters, they were fed into the dynamic model, eq.(1), to estimate the swimming velocity of the robot in a working condition not used in the identification phase. The velocities predicted by the model in the identification and testing conditions are compared with real ones in Fig. 9(b) and Fig. 10(b), where the employed thrust signal is also shown, Fig. 9(a) and Fig. 10(a). The identification set and the two test

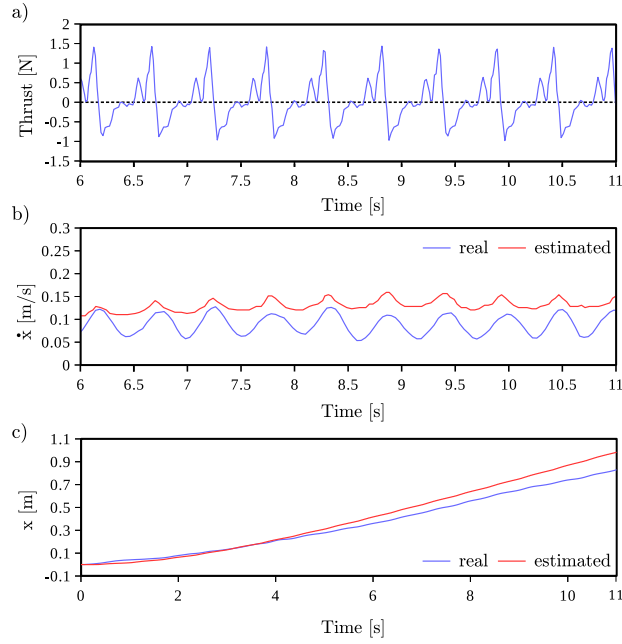


Figure 10. Swimming phase testing set: (a) pulsed-jet thrust input signal for the identification; (b) surge speed at quasi-steady swimming regime; (c) CoM surge displacement throughout the whole experiment.

sets are characterized by different actuation frequencies of the pulsed-jet thrust, respectively 11.47 and 11.76 rad/s. The error between the estimated and real velocities was then calculated for the identification and the test data. A statistical analysis of the velocity error was conducted by calculating the statistical indexes reported in the Table 2, where *mean*, *std* and *max* respectively represent the error average value, standard deviation and maximum error values. Prediction of the CoM displacement throughout the whole duration of the experiments and based on the identified parameters is reported in Fig. 9(c) and Fig. 10(c).

Table 1. Identified parameters for the swimming phase: added mass and quadratic drag.

	m_{a_s} [kg]	Λ [kg/m]
$\hat{\theta}$	2.768	5.094
$\hat{\sigma}_\theta$	0.0054	0.2424
$p_{\hat{\theta}}$	1.9%	16.76%

4.3. Crawling dynamics identification

While crawling, the robot dynamically interacts not only with the fluid, but also with the substrate. As a consequence, beside drag and added mass, additional parameters describing the mechanical properties of the legs and their interaction with the substrate must be

Table 2. Accuracy of the identification procedure for the swimming phase based on the error between the real and predicted velocities from the training and test sets.

	Training	Test set
<i>mean</i> [%]	17.6	31.5
<i>std</i> [%]	61.1	54.4
<i>max</i> [%]	13.9	12.3

accounted for. These quantities will be subject to parameters estimation.

The locomotion of the robot is mainly planar i.e. the CoM approximately moves along the xy plane. A simplified sagittal model was thus developed, instead of one that accounts for all the degrees of freedom of the real robot. The model comprises a central body with three DoF (two translations, one rotation) and four legs, all of which are immersed in water, Fig. 3. Each compliant leg is dynamically modelled as a massless spring-damper system, whose kinematics is derived from the three-bar mechanism described in [24]. Dynamics equations are detailed below:

$$\tilde{m}_c \ddot{x} = \left[\sum_{n=0}^4 t_n (F_{k_x} + F_{c_x})_n + \bar{t}_n (F_{t_x} + F_{n_x})_n \right] + F_{dr_x} \quad (10)$$

$$\tilde{m}_c \ddot{y} = \left[\sum_{n=0}^4 t_n (F_{k_y} + F_{c_y})_n + \bar{t}_n (F_{t_y} + F_{n_y})_n \right] + F_{dr_y} + F_g + F_b \quad (11)$$

$$J \ddot{\vartheta}_0 = \left[\sum_{n=0}^4 t_n (M_k + M_c)_n + \bar{t}_n (M_s)_n \right] + M_b + M_{dr} \quad (12)$$

Eq.(10, 11) account for the translations experienced by the robot in the sagittal (xy) plane. On the left hand side (LHS) of these equations, $\tilde{m}_c = M + m_{a_c}$ represents the effective mass during crawling, which differs from the swimming effective mass due to the crawling added mass term m_{a_c} , to be determined.

The right hand side (RHS) terms in square brackets in Eq.(10, 11) account for reaction forces arising from ground contacts (F_k , F_c) and fluid resistance, referred to here as *sculling* forces, (F_t , F_n).

The reaction forces have an elastic (F_k) and a damping (F_c) component. For example, in the x direction, $F_{k_x} = k \, d\epsilon_x$, while $F_{c_x} = c \, d\dot{\epsilon}_x$, with $d\epsilon_x$ representing the compression state of the limb in x . The terms k and $c = 2 \, dr \sqrt{kM}$, to be determined via identification, respectively represent the elastic and

damping coefficients. Additional parameters (to be identified) related to the interaction of the limbs with the ground are the static (μ_s) and dynamic (μ_d) friction coefficients, which do not appear in these equations (see [24] for additional details).

The viscous drag experienced by each of the four limbs is divided in a tangential (F_t) and normal (F_n) component (relative to the radial axis of the arm), which depend, respectively, on the associated tangential (λ_t) and normal (λ_n) drag coefficients, as in [36]. The viscous term of each individual limb (sculling forces) is summed to the force F_{dr} , which accounts for the drag experienced by the central body as it moves along the surge and heave directions. For example, in the x direction, $F_{dr_x} = \frac{\Lambda_t}{2} \dot{x}|\dot{x}|$. The drag coefficients Λ_t , λ_t and λ_n are all to be determined via identification.

The t_n coefficients, updated by a routine detecting collisions between each limb and the ground, determine which forces act on the body at a given instant in time. When a limb is in contact with the ground ($t_n = 1$, $\bar{t}_n = 0$) reaction forces are included and sculling forces are neglected. When a limb is detached from the ground ($t_n = 0$, $\bar{t}_n = 1$), contact forces are not computed, with sculling forces being accounted for instead.

Dynamics in the vertical direction y , eq.(11), include body forces such as gravity (F_g) and buoyancy (F_b). These depend on the mean density of the robot (ρ_r) which in turn accounts for both material properties and extent of inflation of the buoyancy module. The incorporation of the separation distance b between the CoM and the CoB and their relative orientation β with respect to the median plane (Fig. 3) enables to account for dynamics that are peculiar to underwater legged locomotion [25, 24].

Finally, eq.(12) describes the torques about the axis z orthogonal to the sagittal plane, determining the pitch of the robot (ϑ_0). The quantity J which appears in the LHS of the equation represents the aggregate inertia of the body. Relevant moments appearing in the RHS are M_k , M_c , M_s , M_b which respectively represent the moments arising from elastic, damping, sculling and buoyancy forces. An additional term M_{dr} which accounts for viscous forces acting against body rotations about the z axis is also taken in consideration.

A summary of the relevant parameters to be estimated for the crawling phase is reported in Tab. 3. Since the equations governing the crawling phase are not available in closed form, nor are they linear in the parameters, the parameter estimation optimization problem was solved using Genetic Algorithms (GAs) [37]. The objective of the optimization process is to find the set of unknown model parameters that minimizes the discrepancy between the model and the

experimental reference data, which in this case consists of tracks of the CoM acquired during tank experiments (section 3). The GA-based identification procedure is executed as described below.

Pre-processing and filtering: among the experiments described in section 3, the ones in which the robot exhibited the faster and more stable locomotion were selected. These correspond to the case of a mean robot density $\rho_r = 1238 \text{ kg}\cdot\text{m}^{-3}$. In order to reduce the effects of measurement noise, CoM trajectories were treated with a Savitzky-Golay low-pass filter.

Features extraction and optimization target: the behavior of the robot during each test was characterized based on a series of locomotion-specific features which include the amplitude (a), frequency (f), and mean displacement (\bar{y}) of the CoM heave oscillations, along with the mean surge crawling speed (\bar{x}): the comparison between predicted and recorded trajectories is thus performed within a four dimensional features space. To compute the optimization target, features were extracted based on the last 5 s of tank testing, i.e. when quasi-steady regime had been attained, and averaged over all the trials performed in the selected configuration. The resulting target features vector is,

$$f_T = (a^*, f^*, \bar{x}^*, \bar{y}^*) \\ = (0.0074045 \text{ m}, 1.9831 \text{ Hz}, 0.0403 \text{ m/s}, 0.1272 \text{ m})$$

Formulation and parameters encoding: the parameters estimation was performed as a real-coded bounded minimum optimization problem. The genome,

$$\mathbf{G} = (k, dr, \mu_s, \mu_d, m_{ac}, J, \Lambda_t, \Lambda_r, \lambda_t, \lambda_n)$$

was formulated based on direct encoding, i.e. parameters explicitly appear in the genome.

Parameter bounds: parameters bound were defined according to physically plausible limit cases.

Table 3. Parameters to be estimated for the crawling phase, their allowed range of variability, and the output values of the identification procedure.

	Bound	Value
k [N/m]	[25, 400]	205.8
dr	[0, 1.5]	1.1
μ_s	[0.6, 0.9]	0.77
μ_d	[0.6, 0.9]	0.61
m_{ac} [kg]	[0.755, 7.55]	6.65
J [kg m ²]	[0.0003, 0.018]	0.018
Λ_t [kg/m]	[0.11, 145]	63.6
Λ_r [kg/m]	[0.0001, 1]	0.068
λ_t [kg/m]	[0, 0.08]	0.026
λ_n [kg/m]	[0, 0.3]	0.033

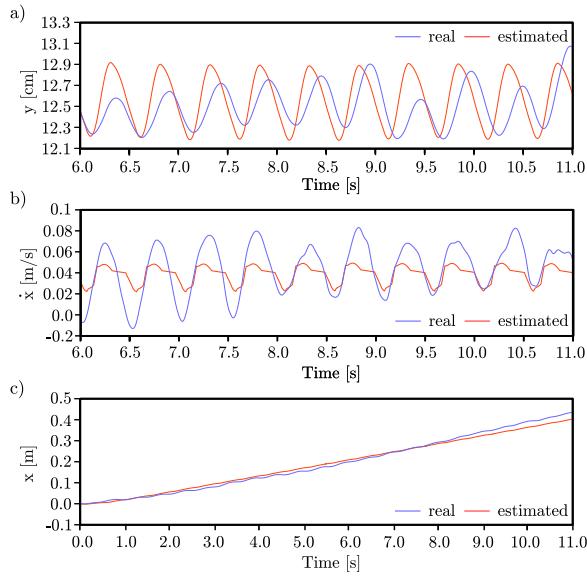


Figure 11. Comparison between tank experiments and output from equations integration based on the identified parameters for the training case, $\rho_r = 1238 \text{ kg} \cdot \text{m}^{-3}$: (a) heave oscillations of the CoM, (b) surge speed at quasi-steady crawling regime and (c) CoM surge displacement throughout the whole experiment.

As an example, the lower bound for the body drag coefficient Λ_t is that of a streamlined body with a circular reference cross section of radius 30 mm, while the upper bound is that of a circular cylinder capable of enclosing the entirety of the robot. Similar considerations concern the definition of the other bounds. In the case of the tangential and normal drag coefficients of the legs, data from studies on the sculling of tapered conical shapes was used [36].

Fitness function: for each genome \mathbf{G} , the features vector f_G is estimated, and the resulting fitness is computed as the sum of normalized squared errors with respect to the target features vector. The fitness function, $f(\mathbf{G})$, is cast as follows:

$$f(\mathbf{G}) = \begin{cases} P_{fall} & \text{if robot fell,} \\ \sum_{i=1}^4 \left(\frac{f_T - f_G}{f_T} \right)^2 & \text{otherwise,} \end{cases} \quad (13)$$

where P_{fall} is a penalty term assigned to choices of the unknown model parameters which cause the simulated model to fall to the ground. A fixed positive penalty of 100 is assigned, plus an additional penalty that depends on how much time the simulated robot managed not to fall, i.e.,

$$P_{fall} = \lceil 100 + 5 \cdot (t_e - t_{fall}) \rceil,$$

where t_e is the total expected execution time and t_{fall} is the instant when falling occurs. Operators in the bottom branch of the assignment, eq.(13), are intended as element-wise vector operators, f_T is

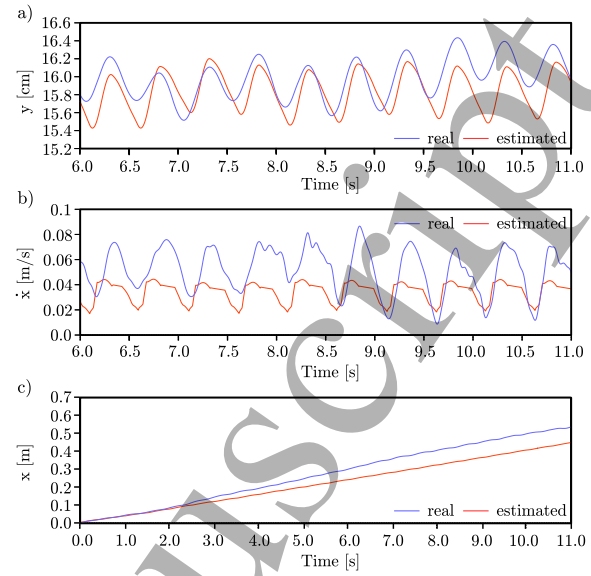


Figure 12. Comparison between tank experiments and output from equations integration based on the identified parameters for the testing case, $\rho_r = 1178 \text{ kg} \cdot \text{m}^{-3}$: (a) heave oscillations of the CoM, (b) surge speed at quasi-steady crawling regime and (c) CoM surge displacement throughout the whole experiment.

the target features vector, and f_G is the features vector characterizing the behavior of the robot for the parameters \mathbf{G} .

Experiments: for each choice of the unknown parameters the equations were integrated over $t_e = 25 \text{ s}$. In analogy with tank experiments, features were extracted in a regime window constrained to the last 5 s of execution.

Testing: after the estimation procedure (training stage) the output parameters were tested in a different operative condition (testing stage), not used during the training and compared with tank experiments performed in the same conditions.

4.4. Crawling phase results

Parameters estimated by the genetic algorithm are reported in Tab. 3. The outcome features vector from the best genome is

$$f_G = (a, f, \bar{x}, \bar{y}) = (0.0074043 \text{ m}, 1.9829 \text{ Hz}, 0.040302 \text{ m/s}, 0.12719 \text{ m})$$

entailing a discrepancy with respect to the target f_T of $2.012 \cdot 10^{-8}$. To compare the behavior of the model against the one of the robot, the characteristic oscillation of the CoM in the y axis is analysed, Fig. 11(a) and 12(a). The forward speed \dot{x} and position x are reported as well for each case, Fig. 11(b-c) and 12(b-c).

In Fig. 11(a) the CoM track of the model simulated with the estimated parameters is overlapped

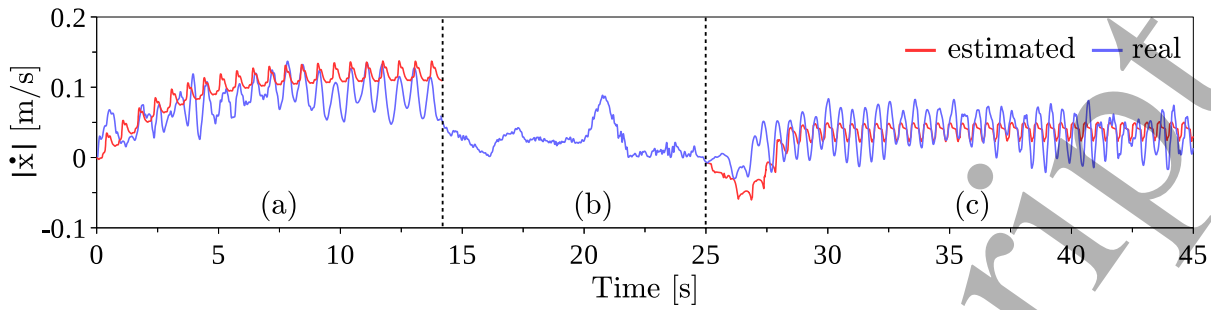


Figure 13. Vehicle surge speed during swimming (a), diving (b) and crawling (c) stages of the locomotion test case. From $t = 15$ s to $t = 25$ s (diving phase) no model predictions are available, thus recorded data are reported only.

onto a tank experiment which exhibits the same robot average density $\rho_r = 1238 \text{ kg} \cdot \text{m}^{-3}$ (the one used for the estimation procedure, i.e. the training condition). The accuracy of the estimated parameters is subsequently assessed via the comparison against a testing condition (i.e. not used during the parameters estimation phase), where $\rho_r = 1178 \text{ kg} \cdot \text{m}^{-3}$, and compared with tanks experiments performed with this reference density. Table 4 summarizes errors and standard deviation arising from the comparison of the position signals, computed on a regime window of 5s.

Table 4. Crawling phase parameters estimation: errors computed from the comparison between the real position profiles and those achieved with estimated parameters

	Training	Test
<i>mean</i> [%]	1.5	1.5
<i>std</i> [%]	4.3	3.5
<i>max</i> [%]	1.0	0.8

5. Discussions

The identification was performed on a training set and compared against the locomotion analysis at quasi-steady regime. Surge speed was used as the fitting criteria for the swimming phase, while a number of features describing heave oscillations of the CoM, as well as the surge speed, were used for the crawling, where the robot exhibits more complex dynamics. Subsequently, the estimated parameters were used to predict the vehicle dynamics in a different configuration from that of the training set. This was done both at quasi-steady, Fig. 10 and 12, and during transitory regime, Fig. 13.

The values identified for the swimming dynamics suffer of a fairly significant mean error, in particular for what concerns the test set, see table 2. In addition, the percentile parameter error is significantly high for the quadratic drag coefficient, though this

value falls within the range encountered in [35]. Our current identification highlights critical inaccuracy for what concerns the drag coefficient Λ , as opposed to [35], where larger $p_{\hat{\theta}}$ values are associated with added mass estimation. This highlights two major problems with the present identification procedure. First, the mismatch between estimated and measured surge speed could depend on the experiment being affected by tank walls wave reflections which slow down the vehicle in the terminal stage of the swimming trial, see Fig. 10(b). However, the major criticism lies in the use of the static thrust as the input signal to eq.(1), i.e. measured with the robot being held still. Thrust estimation from static experiments neglects effects associated with shape change, which can lead to underestimating thrust for as much as 30% of the actual value when the vehicle is freely swimming, [13]. This in turns causes the quadratic drag coefficient to be underestimated as well. When the Λ identified in this way is used to predict the vehicle dynamics, the output surge speed appears overestimated, see Fig. 10(b). While consistent results are observed prior to quasi-steady regime attainment, Fig. 13, CoM surge displacement is found to quickly drift from the observed data, Fig. 10(c).

In the crawling phase, estimated parameters enable a closer match between the robot and the model, both in training and testing condition (Fig. 11(a) and 12(a), Tab. 4). The good qualitative and quantitative match in the testing condition suggests that the parameters are not dramatically overfitted to the identification data, and the model is actually capable of generalizing to unseen circumstances. Some discrepancies are however observed between the predicted and the measured crawling surge speed (Fig. 11(b) and 12(b)) and CoM surge displacement (Fig. 12(c)). Although the number of involved parameters and their interactions makes it hard to infer the individual responsibilities of each term in the overall prediction accuracy, a number of potential causes for these discrepancies could be identified,

corresponding to simplifying assumptions made in the design of the crawling model, as well as during the identification procedure. First, the sagittal model deliberately neglects some of the DoF of the robot. It is possible that some of the dynamics currently being overlooked by the model (such as rolling oscillations) do in fact play a more relevant role than expected in the overall body dynamics. Another considerable simplification lies in how the flexible limbs were abstracted in the model (as massless linear spring-damper systems). In particular, the complex dynamics of the distal part of each limb (silicone cone in Fig. 3) are overlooked. Additionally, ground collisions are modeled as punctual impacts of the spring-damper system with the substrate, while in reality they occur as distributed interactions along an extended contact area arising from the sprawling of each soft silicone limb onto the ground. Similarly, the observed discrepancies may arise from an overly simplistic friction model (detailed in [24]). Limbs can occasionally flex outside the sagittal plane, and their passive dynamics while freely moving in the fluid could affect sculling forces [36], which are known to play a relevant role in the locomotion of this robot [24]. The drag experienced by the buoyancy module (Fig. 5) is implicitly aggregated with the one affecting the main body, which is potentially overly simplistic given the spatial separation and relative size of the two objects. Border effects could also play a relevant role when the robot translates close to the substrate.

Finally, the identification procedure currently uses data from a single experimental trial and operative condition, with other trials being used for testing purposes only: better generalization performances could be achieved by making use of data from more than one trial during the parameters estimation phase. This could be achieved in our setting by simultaneously minimizing the model-data discrepancy in a number of different operative conditions, either defining an aggregate fitness function or by employing truly multi-objectives optimization schemes, which are easily supported by genetic algorithms.

The comparison of the estimated values for swimming and crawling regimes confirms that both the added mass (2.768 kg vs 6.65 kg) and the ensemble quadratic drag coefficient (5.094 kg m^{-1} vs 63.6 kg m^{-1}) are markedly different, as anticipated by observing the kind of interactions taking place between the vehicle and its surroundings (section 4). This supports our choice of performing the parameters identification procedure in a segregated fashion for the two operative conditions.

In spite of the aforementioned limitations, the identified parameters enable the models to predict the overall vehicle behavior in a realistic locomotion

experiment such as that presented in Fig. 5, where the early non-stationary regime is accounted for, Fig. 13. This demonstrates that the procedure employed hereby could be extended to deal with controllers design or path and mission planning. The results are also of importance for simulation-driven studies targeting design improvements [38, 28, 29], based on evolutionary techniques [39] or other bioinspired principles [40, 41].

6. Conclusions

In this paper we have introduced an octopodes-inspired aquatic soft robot capable of shape-changing pulsed-jet propulsion and benthic legged-locomotion. This represents the first example of a new generation of soft multi-modal vehicles which could complement the capabilities of commercial underwater robots by comfortably navigating in cluttered and fragile submerged environments currently precluded to both robots and divers.

The vehicle's highly unconventional morphology and unsteady modes of underwater propulsion has required us to undertake an *ad-hoc* identification procedure aimed at addressing the multi-modal nature of its locomotion. This was based on a hybrid Least Squares/Genetic Algorithm-based experimental determination which supports the uncoupled characterization of the robot dynamics during swimming and crawling. While this approach has been found to work satisfactorily for the crawling regime, the results highlight that accurate experimental characterization of shape-changing pulsed-jet self-propelled vehicles cannot be performed by relying on static thrust input signals alone. The employment of static thrust measurement, where shape-change-driven effects are neglected [13], eventually can yield an underprediction of the estimated quadratic drag coefficient as large as $\sim 50\%$.

However, segregated parameter identification can be regarded as a sound methodology to reliably address the need to experimentally characterize new breeds of unconventional multi-modal vehicles, [42].

As the interest for multi-modal bioinspired vehicles increases [42], the need to derive a reliable dynamics characterization of these morphologically complex and unconventional machines is deemed to become of primary importance. Despite its limitations, the segregated parameter identification presented here can be regarded as a sound methodology to address this requirement.

Acknowledgments

This work was partly supported by the Natural Environment Research Council (grant number

NE/P003966/1) and the Lloyds Register Foundation.

7. References

- [1] L. L. Whitcomb, "Underwater robotics: out of the research laboratory and into the field," in *IEEE International Conference on Robotics and Automation ICRA'00*, pp. 709–716, 2000.
- [2] J. Elvander and G. Hawkes, "Rovs and auvs in support of marine renewable technologies," in *MTS/IEEE Oceans 2012*, (Hampton Roads, VA), pp. 1–6, 2012.
- [3] I. Vasilescu, C. Detweiler, M. Doniec, D. Gurdan, S. Sosnowski, J. Stumpf, and D. Rus, "Amour v: A hovering energy efficient underwater robot capable of dynamic payloads," *The International Journal of Robotics Research*, vol. 29, pp. 547–570, 2010.
- [4] F. S. Hover, R. M. Eustice, A. Kim, B. Englot, H. Johannsson, M. Kaess, and J. J. Leonard, "Advanced perception, navigation and planning for autonomous in-water ship hull inspection," *The International Journal of Robotics Research*, vol. 31, pp. 1445–1464, 2012.
- [5] M. S. Triantafyllou, G. D. Weymouth, and J. Miao, "Biomimetic survival hydrodynamics and flow sensing," *Annual Review of Fluid Mechanics*, vol. 48, pp. 1–24, 2016.
- [6] R. J. Lock, R. Vaidyanathan, S. C. Burgess, and J. Loveless, "Development of a biologically inspired multi-modal wing model for aerial-aquatic robotic vehicles through empirical and numerical modelling of the common guillemot, *Uria aalge*," *Bioinspiration & Biomimetics*, vol. 5, 2010.
- [7] K. H. Low, T. Hu, S. Mohammed, J. Tangorra, and M. Kovac, "Perspectives on biologically inspired hybrid and multi-modal locomotion," *Bioinspiration & Biomimetics*, vol. 10, 2015.
- [8] A. D. Marchese, C. D. Onal, and D. Rus, "Autonomous soft robotic fish capable of escape maneuvers using fluidic elastomer actuators," *Soft Robotics*, vol. 1, pp. 75–87, 2014.
- [9] S. Kim, C. Laschi, and B. Trimmer, "Soft robotics: a bio-inspired evolution in robotics," *Trends in biotechnology*, 2013.
- [10] A. Arienti, M. Calisti, F. Giorgio-Serchi, and C. Laschi, "Poseidrone: design of a soft-bodied rov with crawling, swimming and manipulation ability," in *Proceedings of the MTS/IEEE OCEANS, San Diego, USA, 21-27 September*, MTS/IEEE, 2013.
- [11] F. Corucci, N. Cheney, H. Lipson, C. Laschi, and J. Bongard, "Evolving swimming soft-bodied creatures," in *ALIFE XV, The Fifteenth International Conference on the Synthesis and Simulation of Living Systems, Late Breaking Proceedings*, p. 6, 2016.
- [12] V. Cacucciolo*, F. Corucci*, M. Cianchetti, and C. Laschi, "Evolving optimal swimming in different fluids: A study inspired by batoid fishes," in *Biomimetic and Biohybrid Systems*, pp. 23–34, Springer, 2014.
- [13] G. D. Weymouth, V. Subramaniam, and M. S. Triantafyllou, "Ultra-fast escape maneuver of an octopus-inspired robot," *Bioinspiration & Biomimetics*, vol. 10, 2015.
- [14] F. Giorgio-Serchi and G. D. Weymouth, "Drag cancellation by added-mass pumping," *Journal of Fluid Mechanics*, vol. 798, pp. R3, 1–11, 2016.
- [15] J. M. Gosline and M. E. DeMont, "Jet-propelled swimming squids," *Scientific American*, vol. 252, pp. 96–103, 1985.
- [16] M. Krieg and K. Mohseni, "Modelling circulation, impulse, and kinetic energy of starting jets with non-zero radial velocity," *Journal of Fluid Mechanics*, vol. 719, pp. 488–526, 2013.
- [17] F. Giorgio-Serchi, A. Arienti, and C. Laschi, "A soft unmanned underwater vehicle with augmented thrust capability," in *Proceedings of the MTS/IEEE OCEANS, San Diego, USA, 21-27 September*, MTS/IEEE, 2013.
- [18] P. S. Krueger, "Measurement of propulsive power and evaluation of propulsive performance from the wake of a self-propelled vehicle," *Bioinspiration and Biomimetics*, vol. 1, pp. 49–56, 2006.
- [19] F. Giorgio-Serchi, A. Arienti, and C. Laschi, "Underwater soft-bodied pulsed-jet thrusters: actuator modelling and performance profiling," *International Journal of Robotics Research*, 2016.
- [20] F. Corucci, N. Cheney, H. Lipson, C. Laschi, and J. Bongard, "Material properties affect evolution's ability to exploit morphological computation in growing soft-bodied creatures," in *ALIFE XV, The Fifteenth International Conference on the Synthesis and Simulation of Living Systems*, pp. 234–241, MIT press, 2016.
- [21] M. H. Raibert, *Legged robots that balance*. The MIT Press, 1986.
- [22] F. Iida, J. Rummel, and A. Seyfarth, "Bipedal walking and running with spring-like biarticular muscles," *Journal of biomechanics*, vol. 21, pp. 656–667, 2008.
- [23] S. Floyd and M. Sitti, "Design and development of the lifting and propulsion mechanism for a biologically inspired water runner robot," *IEEE Transaction on robotics*, vol. 24, no. 3, pp. 698–709, 2008.
- [24] M. Calisti, F. Corucci, A. Arienti, and C. Laschi, "Dynamics of underwater legged locomotion: modeling and experiments on an octopus-inspired robot," *Bioinspiration & Biomimetics*, vol. 10, no. 4, p. 046012, 2015.
- [25] M. Calisti, F. Corucci, A. Arienti, and C. Laschi, "Bipedal walking of an octopus-inspired robot," in *PCNS*, Springer, 2014.
- [26] M. Calisti, F. Corucci, A. Arienti, and C. Laschi, "Bipedal walking of an octopus-inspired robot," in *Biomimetic and Biohybrid Systems*, pp. 35–46, Springer, 2014.
- [27] M. Giorrelli, F. Giorgio-Serchi, and C. Laschi, "Forward speed control of a pulsed-jet soft-bodied underwater vehicle," in *Proceedings of the MTS/IEEE OCEANS, San Diego, USA, 21-27 September*, MTS/IEEE, 2013.
- [28] F. Corucci, M. Calisti, H. Hauser, and C. Laschi, "Evolutionary discovery of self-stabilized dynamic gaits for a soft underwater legged robot," in *Advanced Robotics (ICAR), 2015 International Conference on*, pp. 337–344, 2015.
- [29] F. Corucci, M. Calisti, H. Hauser, and C. Laschi, "Novelty-based evolutionary design of morphing underwater robots," in *Proceedings of the 2015 Annual Conference on Genetic and Evolutionary Computation*, pp. 145–152, ACM, 2015.
- [30] F. Renda, F. Giorgio-Serchi, F. Boyer, and C. Laschi, "Structural dynamics of a pulsed-jet propulsion system for underwater soft robot," *International Journal of Advanced Robotics System*, vol. 12, 2015.
- [31] F. Renda, F. Giorgio-Serchi, F. Boyer, and C. Laschi, "Modelling cephalopod-inspired pulsed-jet locomotion for underwater soft robots," *Bioinspiration & Biomimetics*, vol. 10, 2015.
- [32] L. Ljung, *System Identification (2Nd Ed.): Theory for the User*. Upper Saddle River, NJ, USA: Prentice Hall PTR, 1999.
- [33] P. Ridao, A. Tiano, A. El-Fakdi, C. M., and Z. A., "On the identification of non-linear models of unmanned underwater vehicles," *Control Engineering Practice*, vol. 12, no. 12, pp. 1483 – 1499, 2004.
- [34] F. Giorgio-Serchi, F. Renda, M. Calisti, and C. Laschi, "Thrust depletion at high pulsation frequencies in underactuated, soft-bodied, pulsed-jet vehicles," in *OCEANS 2015 - Genova*, pp. 1–6, May 2015.
- [35] M. Caccia, G. Indiveri, and G. Veruggio, "Modeling

and identification of open-frame variable configuration unmanned underwater vehicles,” *Oceanic Engineering, IEEE Journal of*, vol. 25, pp. 227–240, April 2000.

[36] M. Sfakiotakis, A. Kazakidi, and A. D. Tsakiris, “Octopus-inspired multi-arm robotic swimming,” *Bioinspiration & Biomimetics*, vol. 10, 2015.

[37] M. Gen and R. Cheng, *Genetic algorithms and engineering optimization*, vol. 7. John Wiley & Sons, 2000.

[38] F. Renda, F. Giorgio-Serchi, F. Boyer, and C. Laschi, “Locomotion and elastodynamics model of an underwater shell-like soft robot,” in *2015 IEEE International Conference on Robotics and Automation (ICRA)*, pp. 1158–1165, May 2015.

[39] F. Corucci, “Evolutionary developmental soft robotics: Towards adaptive and intelligent soft machines following nature’s approach to design,” in *Soft Robotics: Trends, Applications and Challenges*, pp. 111–116, Springer International Publishing, 2017.

[40] H. Hauser and F. Corucci, “Morphosis - taking morphological computation to the next level,” in *Soft Robotics: Trends, Applications and Challenges*, pp. 117–122, Springer International Publishing, 2017.

[41] F. Corucci, M. Calisti, H. Hauser, and C. Laschi, “Shaping the body to shape the behavior: a more active role of the morphology in the brain-body trade-off,” in *13th European Conference on Artificial Life (ECAL2015), Late Breaking Proceedings*, pp. 7–8, 2015.

[42] R. J. Lock, S. C. Burgess, and R. Vaidyanathan, “Multi-modal locomotion: from animal to application,” *Bioinspiration & Biomimetics*, vol. 9, 2014.